# Separation delay by optimal streaks

**By M. Karp AND M. J. P. Hack**

## 1. Motivation and objectives

Boundary layers are prone to separation when subjected to adverse pressure gradients. Flow separation often leads to increased pressure drag and decreased lift, resulting in reduced performance of aerodynamic and hydrodynamic vehicles. Separation is particularly relevant for low-Reynolds-number aerodynamics of small unmanned air vehicles, for which laminar flow is the rule rather than the exception. Downstream of the separation point, the inflectional shear layer often triggers early breakdown to turbulence. Although the transition to turbulence induces flow reattachment, thereby reducing the size of the separated region, its adverse effects are increased friction and heat transfer.

Vortex generators have been proposed as a possible passive control device for flow separation, owing to their ability to generate counter-rotating streamwise vortices that enhance mixing and often trigger transition to turbulence, enabling a delay or even prevention of separation (e.g., Pearcey 1961). In fact, vortex generators are effective at delaying separation even for fully turbulent flows (e.g., Schubauer & Spangenberg 1960). While several approaches for the active control of flow separation have been proposed over the years (see, e.g., Greenblatt & Wygnanski 2000, for a review), practical considerations strongly favor a passive approach as pursued in the current study.

In the context of transitional flows, it is now well established that transient growth can allow perturbations to amplify even in exponentially stable settings. Counter-rotating streamwise vortices have been identified as the vortical structures leading to optimal linear transient growth in parallel shear flows (see, e.g., Butler & Farrell 1992). Ellingsen & Palm (1975) have demonstrated that the streamwise component of a three-dimensional streamwise independent disturbance grows linearly with time for an inviscid fluid. Taking into account viscosity, Gustavsson (1991) has shown that the growth is bounded and ultimately overcome by viscous decay. The relevant timescale for the transient growth development is of $O(Re)$ and the maximal energy growth scales with $Re^2$. Here, $Re$ is the Reynolds number, defined as $Re = U_\infty \delta/\nu$, where $U_\infty$ is the free-stream velocity, $\delta$ is the boundary layer thickness and $\nu$ is the fluid kinematic viscosity. The most significant transient growth is achieved through the lift-up mechanism (Landahl 1980), where cross-stream velocity components with an amplitude of $A_0$ generate streamwise disturbances, commonly referred to as streaks, with an amplitude of $ReA_0$. Transient disturbance growth analyses of nonparallel flat plate boundary layers (e.g., Andersson *et al.* 1999; Hack & Moin 2017) identified streamwise vortices as the dominant vortical structures, consistent with parallel flows.

The maximal energy growth scales with $Re^2$, suggesting that for high Reynolds numbers even initially small disturbances may reach amplitudes at which nonlinear effects become apparent. In the linear regime, the optimal disturbance corresponds to anti-symmetric sets of high-speed and low-speed streaks. Nonlinear interactions between the streaks and the streamwise vortices break the symmetry by shifting the high-speed streaks toward the wall and the low-speed streaks away from the wall. The resulting distorted

spanwise mean flow has excess velocity close to the wall and a deficit away from the wall (see, e.g., Ran *et al.* 2018). These nonlinear interactions, commonly referred to as mean flow distortion, might be favorable for separation delay as they reinforce the velocity close to the wall, counteracting the velocity deceleration in that region.

The transient growth mechanism has been utilized by Fransson *et al.* (2006) for delaying transition to turbulence. They used cylindrical roughness elements embedded within the boundary layer, acting as vortex generators, to trigger the formation of streamwise vortices, which generate streaks via the lift-up mechanism. The streaks delay transition since they have a stabilizing effect on exponential Tollmien-Schlichting instabilities, as reported by Cossu & Brandt (2002).

The impact of three-dimensional steady and unsteady disturbances on transition in separation bubbles has been investigated by Marxen *et al.* (2004). They have found that steady perturbations up to 3% did not influence transition, which tends to be dominated by oblique traveling waves. Boiko *et al.* (2008) have studied experimentally the effect of stationary disturbances on the separating flow over a backward-facing step. The streaky disturbances induce a temporal mean flow distortion on the separated flow and promote secondary instabilities. A similar study by Pujals *et al.* (2010) has explored the ability of streaks to delay separation over a three-dimensional bluff body. The spanwise modulation successfully suppresses the recirculation bubble and the overall drag is reduced by approximately 10%.

Marxen *et al.* (2009) investigated the spatial transient growth of steady infinitesimal three-dimensional disturbances in a two-dimensional separating boundary layer subjected to a favorable-to-adverse pressure gradient. They found that transient growth caused by the lift-up effect dominates in the favorable pressure gradient region and slightly downstream separation, whereas a Görtler-type modal instability is observed in the adverse pressure gradient region. In a follow-up study Marxen & Rist (2010) analyzed the differences between forced and unforced laminar separation bubbles induced by an adverse pressure gradient. In the forced case the flow transitioned to turbulence, changing the pressure distribution, thus reducing the size of the separation region and stabilizing the laminar flow upstream of the bubble with respect to small, linear perturbations.

Although the concept of using vortex generators for separation delay is not new, the choice of parameters is often based on trial and error. Moreover, the mechanism for optimal separation delay is poorly understood. To address this gap, we focus on the velocity perturbation induced by the vortex generator. Our aim is to find the optimal perturbation, in a sense that the separation location is delayed as far downstream as possible. The relevance of concepts from linear stability theory to separation delay is explored. More specifically, we examine the effect of disturbances maximizing the linear transient growth and their role in generating a mean flow distortion that augments the shear at the wall. Two different optimization objectives, maximal mean separation location and minimal mean bubble length, are compared. This research brief focuses only on a single spanwise wave number of the disturbance.

## 2. Methodology

We consider the incompressible three-dimensional Navier-Stokes equations. All variables are nondimensionalized by the free-stream velocity and boundary layer thickness at the inlet. The velocity components $u$, $v$ and $w$ correspond to velocities along $x$, $y$ and $z$, the streamwise, wall-normal and spanwise dimensions, respectively.

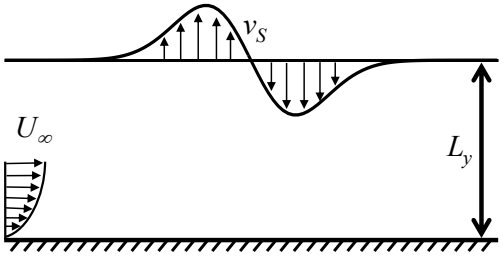


FIGURE 1. Problem setup considered within this work.

Our setting of triggering separation in the flow over a flat plate is similar to that utilized by Na & Moin (1998) and is shown in Figure 1. A suction-injection velocity distribution is prescribed along the upper boundary of the computational domain to create an adverse-to-favorable pressure gradient that produces a closed separation bubble. The vertical velocity distribution is given by

$$v_s(x) = -v_0 \bar{x} \exp\left(\frac{1}{2} - \frac{1}{2}\bar{x}^2\right), \quad \bar{x} = \frac{x - x_s}{\Delta x_s \mathrm{e}^{-1/2}}, \tag{2.1}$$

where $x_s$ is the location where the wall-normal velocity changes sign, $\Delta x_s$ is a representative width of the suction-injection region and $v_0$ is the maximal amplitude. The amount of fluid removed ($x < x_s$) and injected ($x > x_s$) is equal to $v_0 \Delta x_s$.

*Direct numerical simulations*

The flow field is computed in direct numerical simulations using a second-order finite-volume formulation. At the inlet a Blasius profile is superimposed along with a steady disturbance, whose specific details are provided below. The size of the computational domain is $L_x = 200$ in the streamwise direction and $L_y = 30$ in the wall-normal direction. The domain is assumed periodic in the spanwise direction and extends over one disturbance wavelength, $L_z = 2\pi/\beta$, where $\beta$ is the spanwise wave number. An equidistant grid is used along $x$ and $z$, and a hyperbolic tangent clustering with a ratio of $\Delta y_{top}/\Delta y_{wall} = 50$ is employed along the wall-normal direction, leading to a spacing of $\Delta x = 0.1953$, $\Delta z = 0.0982/\beta$ and $\Delta y_{wall} = 0.0084$ for the high-resolution case $(N_x, N_y, N_z) = (1024, 192, 64)$ and a spacing of $\Delta x = 0.3906$, $\Delta z = 0.1963/\beta$ and $\Delta y_{wall} = 0.0126$ for the low-resolution case $(N_x, N_y, N_z) = (512, 128, 32)$. Along the top boundary, a superposition of the Blasius solution and $v_s$ is enforced and a convective condition is prescribed at the outlet. The finite-volume algorithm is based on Rosenfeld *et al.* (1991), with the velocities stored on a staggered grid at the faces of the computational volumes and the pressure stored at their centers. The convective term is integrated in time using a second-order Adams-Bashforth scheme while a second-order Crank-Nicolson scheme is used for the diffusion term. Mass conservation is enforced through the fractional step method of Kim & Moin (1985).

## 3. Laminar separation: Base state

This section describes the base state. The Reynolds number is $Re = 800$ and the parameters for the velocity at the top boundary are fixed to $x_s = 100$, $\Delta x_s = 30$ and $v_0 = 0.2$, for which a laminar separation bubble is formed. The base state has been calculated with the addition of a small-amplitude three-dimensional disturbance at the inlet. The

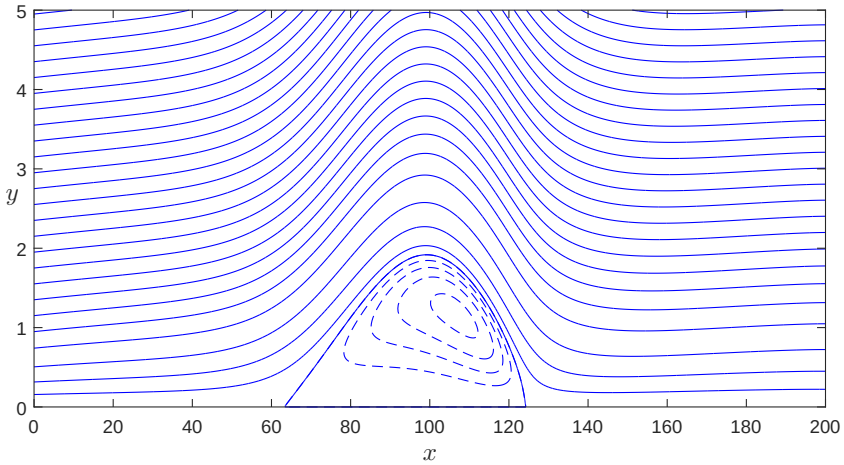


FIGURE 2. Streamlines for a laminar separation bubble, base state. Only the part close to the wall is presented.

disturbance energy is set to $10^{-8}$ in order to trigger a possible absolute instability within the separation bubble. However, such an instability was not observed and the resulting flow remained two dimensional and laminar.

A side view of the streamlines is presented in Figure 2. The dashed lines represent closed streamlines inside the bubble. The maximal bubble height is approximately 2 and its center of recirculation is at $(x, y) = (107, 1.2)$, closer to the reattachment location. The streamwise and wall-normal flow components are shown in Figure 3. Positive (negative) velocities are indicated by the solid (dashed) lines. The free-stream streamwise velocity decelerates to a minimum of 0.71 at $x = x_s$ owing to the adverse pressure gradient. The boundary layer thickens and separates in the adverse pressure gradient region and reattaches in the favorable pressure gradient region. The streamwise component remains negative up to $y = 1.3$, approximately two-thirds of the bubble height. The maximal reverse flow has a magnitude of 6.6%, which is lower than 15-20%, the threshold for the onset of absolute instability suggested by Alam & Sandham (2000). The wall-normal velocity is effectively antisymmetric with respect to $x = x_s$, with positive (negative) velocities upstream (downstream) of the bubble.

The wall shear is indicated by the dash-dotted line in Figure 4(a), with the Blasius solution, given for reference, indicated by the dashed line. The curve initially follows the Blasius solution, and separation occurs at $x = 63$. The laminar separation bubble closes with a laminar reattachment at $x = 124$ and the curve overshoots the Blasius solution. The wall pressure coefficient, given by $c_p = (p_w - p_\infty)/(0.5\rho_\infty U_\infty^2)$, is indicated by the dash-dotted line in Figure 4(b). The dashed line corresponds to the inviscid solution obtained analytically by defining a flow potential, as detailed in the Appendix. The inviscid solution sets an upper bound to the pressure rise on the wall, which could be achieved without separation. Initially, the viscous (dash-dotted line) and inviscid (dashed line) curves rise together; however, upon separation the pressure flattens and remains below the level observed for the inviscid solution. The pressure coefficient attains a maximum of $c_p = 0.18$ close to the reattachment location and is followed by a slow decay, as in the inviscid solution.

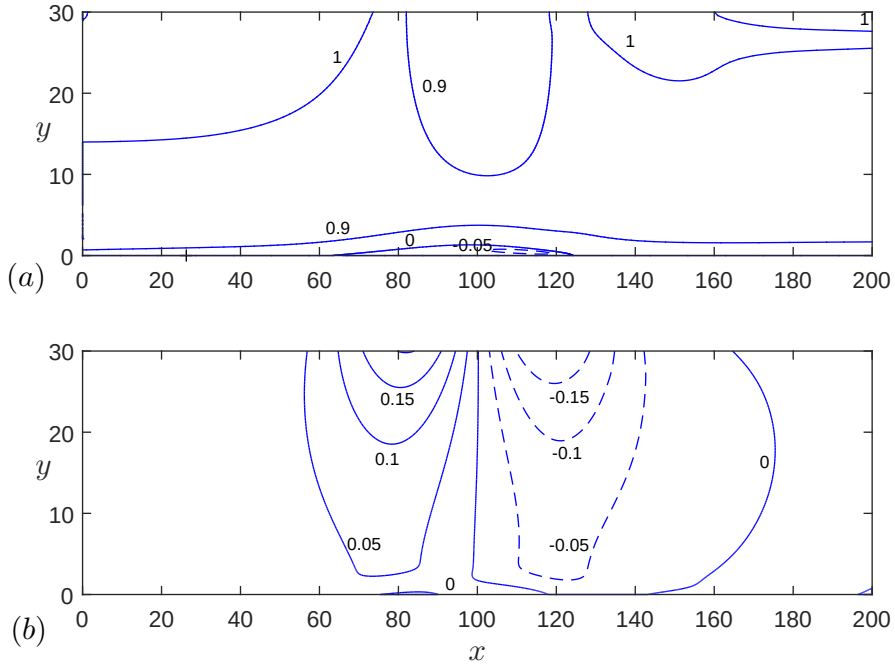


FIGURE 3. Velocity components for a laminar separation bubble, base state. (a) Streamwise. (b) Wall-normal.

## 4. Separation delay using linear transient growth

This section describes the effect of a steady three-dimensional perturbation, obtained from a linear transient growth analysis, on the laminar separation bubble. We employ local spatial stability theory to calculate the linear transient growth. Accordingly, the total velocity is written as

$$\boldsymbol{u}_t = \big(U_B(y), 0, 0\big)^T + \varepsilon \boldsymbol{u}, \tag{4.1}$$

where $U_B(y)$ is the Blasius solution and $\boldsymbol{u}$ is the disturbance. The linearized equations assuming a steady disturbance are

$$U_B \frac{\partial u}{\partial x} + U_B' v + \frac{\partial p}{\partial x} = \frac{1}{Re}\nabla^2 u, \tag{4.2a}$$

$$U_B \frac{\partial v}{\partial x} + \frac{\partial p}{\partial y} = \frac{1}{Re}\nabla^2 v, \tag{4.2b}$$

$$U_B \frac{\partial w}{\partial x} + \frac{\partial p}{\partial z} = \frac{1}{Re}\nabla^2 w, \tag{4.2c}$$

$$\frac{\partial u}{\partial x} + \frac{\partial v}{\partial y} + \frac{\partial w}{\partial z} = 0. \tag{4.2d}$$

The homogeneity of the above base flow in the $x$ and $z$ dimensions allows an ansatz of

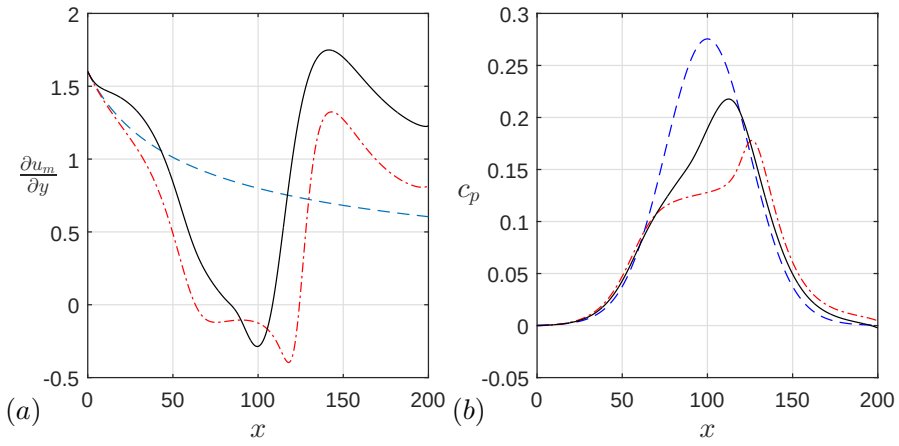


FIGURE 4. Comparison of base (dash-dotted line) and optimized (solid line) states. In the optimized case the inflow perturbation is obtained by local linear transient growth analysis and the inflow energy is $E_0 = 10^{-4}$. (a) Wall shear. Dashed line corresponds to the Blasius solution. (b) Wall pressure coefficient. Dashed line corresponds to the inviscid solution.

the form

$$\boldsymbol{q} = \hat{\boldsymbol{q}}(y)\mathrm{e}^{\mathrm{i}(\alpha x+\beta z)} + (\text{c.c.}), \tag{4.3}$$

where $\boldsymbol{q} = (u, v, w, p)^T$, $\beta$ is the spanwise wave number and $\alpha$ is the spatial complex eigenvalue. The eigenvalue problem is solved by a spectral method and a mapping of the Chebyshev interval $\hat{y} \in [-1, 1]$ to the physical domain $y \in [0, y_{max}]$, such that (Hanifi *et al.* 1996)

$$y = a\frac{1+\hat{y}}{b-\hat{y}}, \quad a = \frac{y_i y_{max}}{y_{max} - 2y_i}, \quad b = 1 + \frac{2a}{y_{max}}, \tag{4.4}$$

which maps half of the grid points to the interval $y \in [0, y_i]$. In the current study 200 Chebyshev polynomials with $y_{max} = 7$ and $y_i = 1.4$ are used.

The linear transient growth is calculated from the gain, $G(x) = E(x)/E_0$, of the disturbance kinetic energy, $E(x) = (\boldsymbol{q}(x), \boldsymbol{q}(x))_E$, at location $x$ normalized by its value at the inflow, $E_0 = E(x = 0)$, with the energy norm given by

$$(\boldsymbol{q}_i, \boldsymbol{q}_j)_E = \frac{1}{2L_z}\int_0^{L_z}\int_0^{\infty}(u_i^* u_j + v_i^* v_j + w_i^* w_j)\,\mathrm{d}y\,\mathrm{d}z, \tag{4.5}$$

where $L_z = 2\pi/\beta$.

The procedure for identifying the optimal solutions is briefly described below, and the reader is referred to Schmid & Henningson (2001) for the details. We begin by solving the eigenvalue problem to obtain the eigenvalues $\alpha$ and the eigenfunctions $\hat{\boldsymbol{q}}(y)$. The variables are written as

$$\boldsymbol{q} = \sum_{n=1}^{\infty} c_n \hat{\boldsymbol{q}}_n(y)\mathrm{e}^{\mathrm{i}(\alpha_n x+\beta z)} + (\text{c.c.}), \tag{4.6}$$

where $\boldsymbol{c}$ are expansion coefficients of the eigenmodes. Next, the energy norm matrix is

calculated

$$M_{i,j} = (\boldsymbol{q}_i, \boldsymbol{q}_j)_E. \tag{4.7}$$

This matrix is Hermitian positive-definite and can be decomposed via Cholesky factorization, $M = F^H F$, where the superscript $H$ implies the Hermitian (conjugate) transpose. This allows connecting the energy norm to the $L_2$ norm via the relation

$$(\boldsymbol{q}_i, \boldsymbol{q}_j)_E = c_i^H M c_j = c_i^H F^H F c_j = (Fc_i, Fc_j)_2. \tag{4.8}$$

The maximal possible amplification is given by

$$G(x) = \max_{\boldsymbol{q}_0} \frac{\|\boldsymbol{q}(x)\|_E^2}{\|\boldsymbol{q}_0\|_E^2} = \max_{\boldsymbol{c}_0} \frac{\|F\boldsymbol{c}(x)\|_2^2}{\|F\boldsymbol{c}_0\|_2^2} = \|Fe^{\mathrm{i}\Lambda x}F^{-1}\|_2^2, \tag{4.9}$$

where $\Lambda = \mathrm{diag}\{\alpha_1, \alpha_2, ...\}$. This procedure gives the envelope for all possible maximum energy amplifications, in which, for each $x$ position, the gain $G(x)$ is optimized over all possible inflow conditions. The specific inflow condition achieving a maximum at a certain $x$ is given by a singular value decomposition of the matrix exponential. Convergence studies showed that 200 eigenmodes are sufficient to capture the optimal growth.

We consider a spanwise wave number of $\beta = 1.85$, for which maximal disturbance energy growth in a zero-pressure-gradient flat plate boundary layer is obtained (e.g., Butler & Farrell 1992). The chosen inflow energy of $E_0 = 10^{-4}$ induces appreciable nonlinear interactions of perturbations. The resulting mean wall shear and coefficient of pressure are indicated by the solid lines in Figure 4. In Figure 4(a) the wall shear is enhanced compared to the base state (dash-dotted line). This effect is attributed to the mean flow distortion during the transient growth, which adds momentum close to the wall. The mean flow distortion can be quantified by considering the same case without separation, i.e., without the suction-injection profile at the top. The result is presented in Figure 5, where positive (negative) mean flow distortion is indicated by the solid (dashed) lines and the dash-dotted line indicates zero. The maximal mean flow distortion is obtained for $y = 0.5$ and a relatively large range of $x$. Returning to Figure 4(a), the mean separation is delayed to $x = 84$ and the mean reattachment moves upstream to $x = 108$, reducing the mean bubble size by 60%. The wall coefficient of pressure in Figure 4(b) does not flatten in the separated region and is much closer to the inviscid distribution with a peak of 0.22.

## 5. Optimal separation delay

In the previous section it was demonstrated that a disturbance obtained from local linear transient growth analysis is able to delay the mean separation by approximately 20 boundary layer thicknesses and reduce the mean bubble size by 60%. In this section we conduct a nonlinear optimization using the method described below. The initial condition from linear transient growth analysis is used as an initial guess for the algorithm and the spanwise wave number remains fixed at $\beta = 1.85$. Results of three different optimizations are presented and compared. First, the optimization objective is set to maximal delay of separation. Second, the optimization objective is set to minimal bubble size. Last, an optimization over all three velocity components is performed with the objective of maximal separation delay.

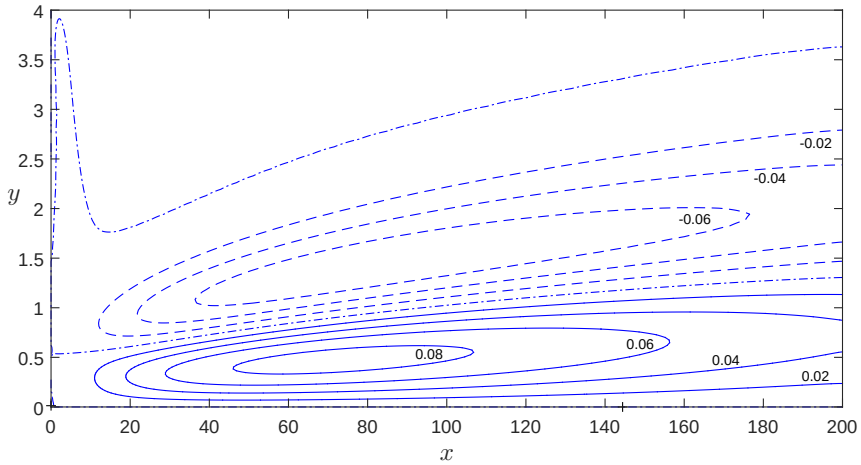


FIGURE 5. Mean flow distortion for a zero-pressure-gradient laminar boundary layer (in the absence of separation). The inflow disturbance is obtained from linear transient growth and the inflow disturbance kinetic energy is $E_0 = 10^{-4}$. Positive (negative) mean flow distortion is indicated by the solid (dashed) lines and the dash-dotted line indicates zero.

### 5.1. *Nonlinear optimization*

The optimal disturbance shape at the inlet is sought such that the point of separation is delayed as far downstream as possible. For a steady disturbance the velocity field at the inlet can be written as

$$u(x=0,y,z) = \hat{u}(s_1, s_2, \ldots, s_N)\cos(\beta z), \tag{5.1a}$$

$$v(x=0,y,z) = \hat{v}(s_1, s_2, \ldots, s_N)\cos(\beta z), \tag{5.1b}$$

$$w(x=0,y,z) = -\hat{w}(s_1, s_2, \ldots, s_N)\sin(\beta z), \tag{5.1c}$$

where $\boldsymbol{s}$ is a vector of the degrees of freedom in the problem. The kinetic energy of the disturbance at the inlet, $E_0$, is enforced by normalizing the disturbance kinetic energy to $E_0$ for each guess. The function of interest for maximization is $x_{sep}$, the spanwise-averaged separation location, given by

$$x_{sep} = \min_x \left\{ \frac{\partial u_m}{\partial y}(x, y=0) = 0 \right\}, \tag{5.2}$$

where $u_m$ is the spanwise mean of the streamwise velocity

$$u_m = \frac{1}{L_z}\int_0^{L_z} u \, \mathrm{d}z. \tag{5.3}$$

The dependence of $x_{sep}$ on $\boldsymbol{s}$ is obtained by solving the Navier-Stokes equations and cannot be written explicitly; thus, the optimization algorithm considered below is fully nonlinear.

In addition to $x_{sep}$, another possible optimization objective that has been analyzed is

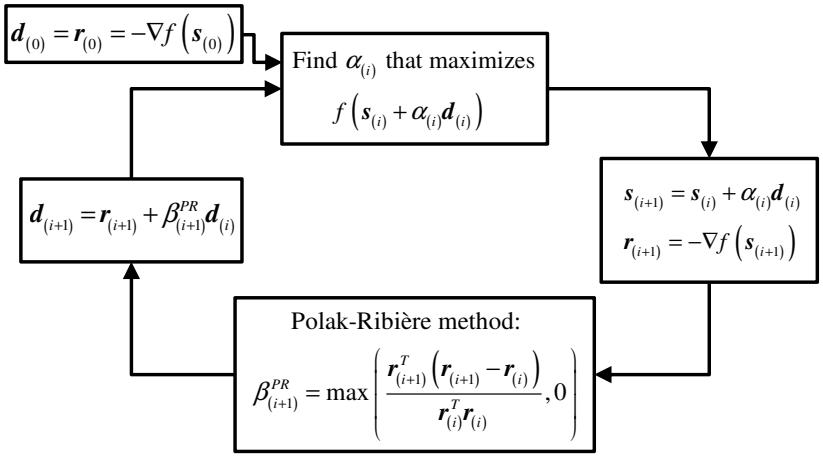


FIGURE 6. Schematic of the optimization algorithm.

the length of the separation bubble (assuming steady reattachment), defined as $L_{bubble} = x_{rea} - x_{sep}$, where $x_{rea}$ is the spanwise-averaged reattachment location, given by

$$x_{rea} = \max_x \left\{ \frac{\partial u_m}{\partial y}(x, y = 0) = 0 \right\}. \tag{5.4}$$

A comparison of the optimal disturbance maximizing $x_{sep}$ and the optimal disturbance minimizing $L_{bubble}$ is presented in Section 5.3.

The optimization is performed by means of the conjugate gradient algorithm described schematically in Figure 6. The iterative loop is initialized by a guess $\boldsymbol{s}_{(0)}$, used to generate the first search direction $\boldsymbol{d}_{(0)}$, which is simply the gradient. The loop begins with a line search to find the maximum of $f(\boldsymbol{s})$ along the direction $\boldsymbol{d}_{(i)}$, leading to the next guess $\boldsymbol{s}_{(i+1)}$. The next search direction, $\boldsymbol{d}_{(i+1)}$, is found by using the Polak-Ribière formula (Polak & Ribière 1969). The convergence criterion is set to less than 1% relative change in the magnitude of the velocity components.

The degrees of freedom were selected as the values of the velocity components at several wall-normal locations. These locations were chosen as the 23 points closest to the wall, which match every third grid point in the low-resolution case ($N_y = 128$), with the outermost point located at $y_{23} = 4.347$. A representative disturbance is plotted by the solid line in Figure 7 and the function values at the 23 locations are indicated by circles. A piecewise cubic spline interpolation was used to reconstruct the function between the points and exponential decay was assumed for $y > y_{23}$. The validity of the reconstruction procedure has been verified by obtaining differences smaller than 1% between the original and reconstructed functions for several representative disturbances. For the optimization algorithm, the no-slip and impermeability boundary conditions were incorporated in the reconstruction procedure and $(\partial v/\partial y)_{wall} = 0$ was enforced by mirroring the $v$ values with respect to the $x$ axis prior to the reconstruction.

The optimization algorithm is able to perform optimization over all three velocity components; i.e., the total number of degrees of freedom is $23 \times 3 = 69$. For optimal disturbances maximizing the transient growth, it is known that the streamwise component is negligible at the initial position, with most of the energy concentrated in the cross-stream components. Therefore, initially only $v$ and $w$ are considered in the optimization,

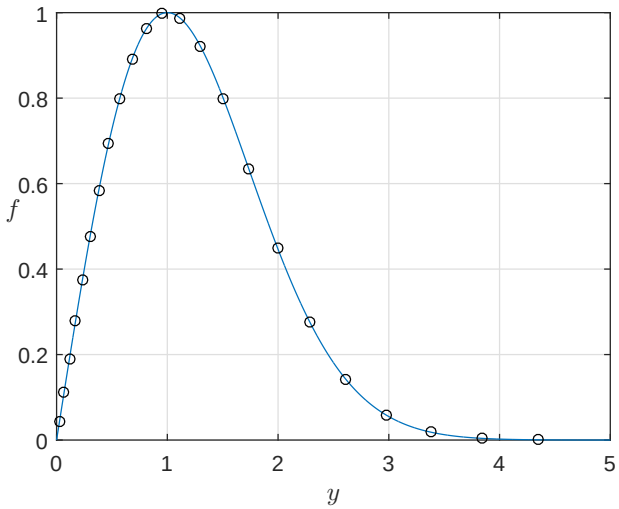


FIGURE 7. Representative disturbance computed by the optimization algorithm. The circles mark the variables chosen for the optimization. The solid line represents the reconstructed function.

reducing the number of degrees of freedom to $23 \times 2 = 46$. The influence of $u$ is addressed in Section 5.4.

### 5.2. *Optimization for maximal separation delay*

Here, results for the maximization of the mean separation location are presented. The resulting optimal disturbance is indicated by the solid lines in Figure 8(a). The initial guess is given for reference and is indicated by the dashed lines. The optimal velocity distribution is more concentrated in the boundary layer and the most significant change is in the maximum of the spanwise component, which changes from 0.015 to 0.021. The effect on the mean wall shear is presented in Figure 9, where Figure 9(b) is a magnification of the separated region in Figure 9(a). The dashed line represents the Blasius solution, the dash-dotted line represents the base state and the solid lines represent the optimized cases. The initial guess based on transient growth is indicated by a plus sign and the optimum for maximal delay of separation is indicated by a cross. The optimal separation location is 85.4 compared with 84 for the classical linear transient growth. Note that initially the transient growth solution generates a larger mean wall shear modification. The reattachment location is delayed to 110 compared with 108 for the transient growth solution, yielding a similar bubble size in both cases. To better understand why the nonlinear optimal disturbance is more effective at delaying separation, it is useful to compare the spanwise distribution of the wall shear in both cases. The wall shear at a representative streamwise location of $x = 80$ is shown in Figure 10, where the dashed and solid lines correspond to the transient growth case and nonlinear optimal disturbance, respectively. It can be seen that the main differences are in the low-speed streak region ($z\beta/\pi = 1$), where the optimum attains smaller negative values. This allows delay of the separation point further downstream compared to the transient growth.

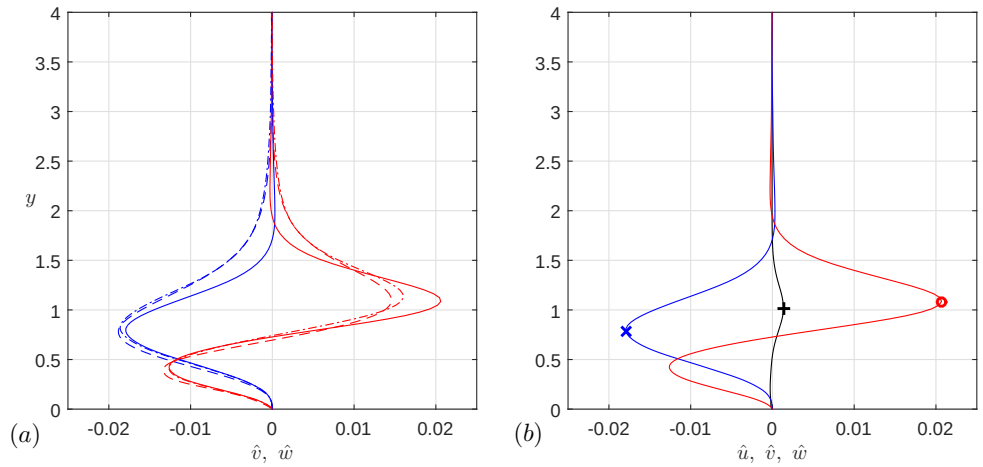


FIGURE 8. Optimal velocity disturbance profiles. (a) Optimization of wall-normal (dark) and spanwise (light) velocity profiles. Solid lines represent the optimum for maximum separation delay, dash-dotted lines represent the optimum for minimal bubble length and dashed lines correspond to the initial guess based on transient growth. (b) Optimization of streamwise (+), wall-normal (×) and spanwise (○) velocity profiles for maximum separation delay.

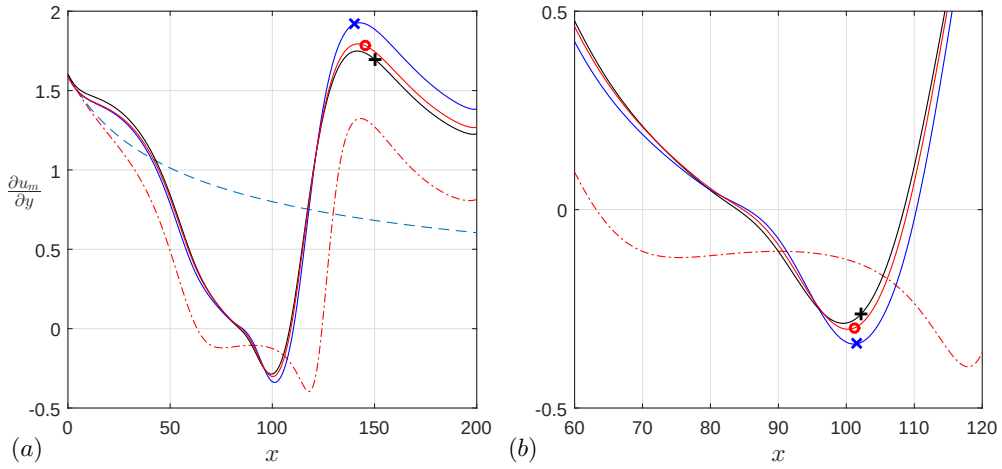


FIGURE 9. A comparison of the mean wall shear in the base state (dashed-dotted line) and optimized cases (solid lines). Initial guess based on transient growth (+), optimum for maximal delay of separation (×) and optimum for minimal bubble size (○). The Blasius solution, given for reference, is indicated by the dashed line. Panel (b) is a magnification of the separated region in panel (a).

### 5.3. *Optimization for minimal bubble size*

In this section the optimization objective is set to minimize the mean bubble size. The resulting optimal disturbance is indicated by the dash-dotted lines in Figure 8(a). The optimal disturbance is similar to the initial guess based on transient growth (dashed lines), with minor differences near the maximum of the spanwise velocity. The resulting mean wall shear is presented in Figure 9, where the optimum for the minimal mean bubble

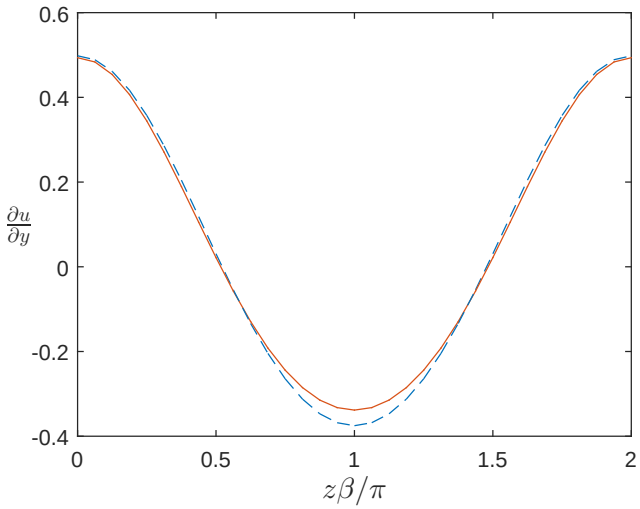


FIGURE 10. Spanwise distribution of wall shear at $x = 80$. Comparison of the inflow perturbation obtained using a local linear transient growth (dashed line) and the optimal disturbance for maximal delay of separation (solid line). The inflow energy is $E_0 = 10^{-4}$.

size is indicated by a circle. A comparison to the reference transient growth curve (solid line marked by a plus sign) again reveals minor differences. The minimal mean bubble size is 24.2, compared with 24.5 for the transient growth. Overall, the results of the optimization for the minimal mean bubble size are thus consistent with the optimization of the mean separation location. We further note that in practice the reattachment of laminar separation bubbles is often turbulent and unsteady, which poses a challenge to the calculation of the mean bubble size.

### 5.4. *Optimization of all three velocity components*

So far, the optimization is performed only on the cross-stream velocity components ($v$, $w$), with the streamwise component assumed negligible. To verify this assumption, an optimization over all three velocity components is performed. The objective is set to the maximal mean delay of separation. The resulting disturbance is presented in Figure 8(b). The maximal magnitude of the resulting streamwise component is very small ($13\times10^{-4}$) and the cross-stream components are practically identical to the ones obtained for the optimization without the streamwise component (solid lines in Figure 8(a)). The improvement in the mean separation location is 0.02, which is negligible. These results confirm that the streamwise component is indeed negligible in the optimization.

## 6. Conclusions

The ability of steady streaks to delay separation has been analyzed by means of nonlinear optimization. The base state corresponds to a two-dimensional steady closed laminar separation bubble enforced by a suction-injection profile along the top boundary of the domain. The optimal inflow disturbance, capable of delaying separation as far downstream as possible, is sought. An initial guess based on maximal linear disturbance transient growth leads to significant delay of the separation and serves as a starting point for the

optimization algorithm. The transient growth analysis also predicts a negligible contribution of the disturbance streamwise component to separation delay, enabling optimization of only the cross-stream components. The mechanism responsible for separation delay is a mean flow distortion, generated by nonlinear interactions during the transient growth stage. The mean flow distortion augments the velocity close to the wall, counteracting the velocity deceleration in that region. Similar results have been obtained for two optimization objectives — maximal mean separation location and minimal mean bubble length.

## Acknowledgments

This investigation was funded by ONR, Grant #N00014-17-1-2341.

## Appendix: Inviscid solution for a two-dimensional flow with suction-injection

This appendix describes the inviscid solution of a uniform flow, subjected to suction-injection along $y = L_y$, with no penetration along the wall at $y = 0$. Assuming irrotational flow, it is useful to define the flow potential $\phi$ such that $u = \partial\phi/\partial x$ and $v = \partial\phi/\partial y$. The resulting governing equation is

$$\nabla^2\phi = 0, \tag{A 1}$$

with the following boundary conditions

$$\phi(\pm\infty, y) = x, \quad \frac{\partial\phi}{\partial y}(x, 0) = 0, \quad \frac{\partial\phi}{\partial y}(x, L_y) = v_s(x), \tag{A 2}$$

where $v_s$ is given in Eq. (2.1). The solution is readily obtained by performing a Fourier transformation along $x$, leading to the following expression for the potential

$$\phi = x - \frac{\mathrm{i}}{\sqrt{2\pi}} v_0 \Delta x_s^2 \mathrm{e}^{-1/2} \int_{-\infty}^{\infty} \mathrm{e}^{-\frac{1}{2}(\alpha\Delta x_s \mathrm{e}^{-1/2})^2 - \mathrm{i}\alpha(x - x_s)} \frac{\cosh(\alpha y)}{\sinh(\alpha L_y)} \, \mathrm{d}\alpha, \tag{A 3}$$

with the corresponding velocity components given by

$$u = 1 - \frac{1}{\sqrt{2\pi}} v_0 \Delta x_s^2 \mathrm{e}^{-1/2} \int_{-\infty}^{\infty} \alpha \mathrm{e}^{-\frac{1}{2}(\alpha\Delta x_s \mathrm{e}^{-1/2})^2 - \mathrm{i}\alpha(x - x_s)} \frac{\cosh(\alpha y)}{\sinh(\alpha L_y)} \, \mathrm{d}\alpha, \tag{A 4}$$

$$v = -\frac{\mathrm{i}}{\sqrt{2\pi}} v_0 \Delta x_s^2 \mathrm{e}^{-1/2} \int_{-\infty}^{\infty} \alpha \mathrm{e}^{-\frac{1}{2}(\alpha\Delta x_s \mathrm{e}^{-1/2})^2 - \mathrm{i}\alpha(x - x_s)} \frac{\sinh(\alpha y)}{\sinh(\alpha L_y)} \, \mathrm{d}\alpha. \tag{A 5}$$

## REFERENCES

Alam, M. & Sandham, N. D. 2000 Direct numerical simulation of 'short' laminar separation bubbles with turbulent reattachment. *J. Fluid Mech.* **410**, 1–28.

Andersson, P., Berggren, M. & Henningson, D. S. 1999 Optimal disturbances and bypass transition in boundary layers. *Phys. Fluids* **11**, 134–150.

Boiko, A. V., Dovgal, A. V. & Hein, S. 2008 Control of a laminar separating

boundary layer by induced stationary perturbations. *Eur. J. Mech. B-Fluid* **27**, 466–476.

Butler, K. M. & Farrell, B. F. 1992 Three-dimensional optimal perturbations in viscous shear flow. *Phys. Fluids A* **4**, 1637–1650.

Cossu, C. & Brandt, L. 2002 Stabilization of Tollmien–Schlichting waves by finite amplitude optimal streaks in the Blasius boundary layer. *Phys. Fluids* **14**, L57–L60.

Ellingsen, T. & Palm, E. 1975 Stability of linear flow. *Phys. Fluids* **18**, 487–488.

Fransson, J. H. M., Talamelli, A., Brandt, L. & Cossu, C. 2006 Delaying transition to turbulence by a passive mechanism. *Phys. Rev. Lett.* **96**, 064501.

Greenblatt, D. & Wygnanski, I. J. 2000 The control of flow separation by periodic excitation. *Prog. Aerosp. Sci.* **36**, 487–545.

Gustavsson, L. H. 1991 Energy growth of three-dimensional disturbances in plane Poiseuille flow. *J. Fluid Mech.* **224**, 241–260.

Hack, M. J. P. & Moin, P. 2017 Algebraic disturbance growth by interaction of Orr and lift-up mechanisms. *J. Fluid Mech.* **829**, 112–126.

Hanifi, A., Schmid, P. J. & Henningson, D. S. 1996 Transient growth in compressible boundary layer flow. *Phys. Fluids* **8**, 826–837.

Kim, J. & Moin, P. 1985 Application of a fractional-step method to incompressible Navier-Stokes equations. *J. Comput. Phys.* **59**, 308–323.

Landahl, M. T. 1980 A note on an algebraic instability of inviscid parallel shear flows. *J. Fluid Mech.* **98**, 243–251.

Marxen, O., Lang, M., Rist, U., Levin, O. & Henningson, D. S. 2009 Mechanisms for spatial steady three-dimensional disturbance growth in a non-parallel and separating boundary layer. *J. Fluid Mech.* **634**, 165–189.

Marxen, O. & Rist, U. 2010 Mean flow deformation in a laminar separation bubble: separation and stability characteristics. *J. Fluid Mech.* **660**, 37–54.

Marxen, O., Rist, U. & Wagner, S. 2004 Effect of spanwise-modulated disturbances on transition in a separated boundary layer. *AIAA J.* **42**, 937–944.

Na, Y. & Moin, P. 1998 Direct numerical simulation of a separated turbulent boundary layer. *J. Fluid Mech.* **374**, 379–405.

Pearcey, H. H. 1961 Shock-induced separation and its prevention. In Lachmann, G. V. (Ed.) *Boundary Layer and Flow Control: Its Principle and Applications.* Pergamon Press.

Polak, E. & Ribière, G. 1969 Note sur la convergence de directions conjugées. *Rev. Fr. Inform. Rech. O.* **16**, 35–43.

Pujals, G., Depardon, S. & Cossu, C. 2010 Drag reduction of a 3D bluff body using coherent streamwise streaks. *Exp. Fluids* **49**, 1085–1094.

Ran, W., Zare, A., Hack, M. J. P. & Jovanovic, M. R. 2018 Low-complexity modeling of mode interactions in boundary layer flows. In *2018 Annual American Control Conference (ACC)*, pp. 134–139.

Rosenfeld, M., Kwak, D. & Vinokur, M. 1991 A fractional step solution method for the unsteady incompressible Navier-Stokes equations in generalized coordinate systems. *J. Comput. Phys.* **94**, 102–137.

Schmid, P. J. & Henningson, D. S. 2001 *Stability and Transition in Shear Flows*. Springer-Verlag.

Schubauer, G. B. & Spangenberg, W. G. 1960 Forced mixing in boundary layers. *J. Fluid Mech.* **8**, 10–32.